ELSEVIER

Contents lists available at ScienceDirect

Cement and Concrete Research

journal homepage: www.elsevier.com/locate/cemconres



Phosphate-activated basic oxygen furnace (BOF) slag: Understanding pH-driven hydration and strength development

Yanjie Tang ^{a,b,*}, Katrin Schollbach ^{a,**}, Zixing Liu ^a, Sieger van der Laan ^a, Wei Chen ^{a,b,*}, H.J.H. Brouwers ^{a,b}

ARTICLE INFO

Keywords: BOF slag Acidic phosphate Alkaline phosphate Hydration pH

ABSTRACT

This study investigates the hydration behavior of basic oxygen furnace (BOF) slag in phosphate solutions across different pH levels, focusing on hydration kinetics, microstructure, and strength development. Acidic phosphate solutions trigger rapid dissolution via acid-base reactions, resulting in lower heat release, while alkaline phosphates promote sustained dissolution-precipitation reactions, prolonging hydration and increasing cumulative heat. The buffering effect of $\rm H_2PO_4^-/HPO_4^2^-$ prolongs induction periods and inhibits hydrogarnet and layered double hydroxides (LDHs) formation. At early stages, $\rm C_2S$ hydration is more pronounced in acidic solutions, whereas higher pH enhances late-stage hydration of $\rm C_2S$, brownmillerite, and wuestite, forming C-S-H, hydrogarnet, and LDHs. Despite similar porosities (11.9–13.9 %), strengths vary from 37.7 to 66.9 MPa due to a higher proportion of capillary pores and a larger average pore size at a low pH (pH at 4.2). The findings support using phosphate-rich wastewater to activate BOF slag, reducing phosphate discharge while developing low-carbon, cement-free binders.

1. Introduction

Industrial and nuclear wastewater streams often contain high concentrations of dissolved phosphates, which pose significant environmental challenges if not properly managed [1]. However, these phosphate-rich wastewaters present an opportunity for sustainable valorization in construction materials. Instead of being treated as pollutants, concentrated phosphate solutions can be repurposed as chemical activators for steel slag, offering a dual environmental benefit in reducing phosphate discharge into aquatic ecosystems and enhancing the reactivity of steel slag to develop low-carbon, cement-free binders [2,3].

Phosphates are commonly recognized as set retarders in Portland cement, where they inhibit the hydration of alite (C_3S) and tricalcium aluminate (C_3A) due to calcium complexation and surface adsorption, etc. [4–6]. However, in steel slag, which primarily consists of dicalcium silicate (C_2S) and brownmillerite $(C_2(A,F))$, phosphates exhibit a fundamentally different behavior since the inherent hydraulic activities

of C_2S and $C_2(A,F)$ are significantly lower than those of C_3S and C_3A [2,3,7]. Recent studies have demonstrated that phosphate activation can enhance the hydration of steel slag by promoting the formation of layered double hydroxides (LDHs), hydrogarnet, and calcium silicate hydrate (C-S-H) gel as dominant hydration products, thereby achieving satisfactory mechanical performance of steel slag binders (28d compressive strength >40 MPa) [2,7]. This suggests that phosphate-rich industrial waste streams could serve as effective activators for steel slag, reducing the reliance on conventional alkali activators while simultaneously addressing phosphate pollution.

While phosphate-based activation of steel slag has been previously explored, the influence of phosphate activation across a broad pH range remains largely unexamined. In cement chemistry, the hydration behavior differs with respect to reaction kinetics, reaction products and strength development for different pH. Under varying pH conditions (pH = 3, 7 and 12) with Portland cement, the hydration products generally remain the same, however the quantities of products are different, e.g. portlandite increases with rising pH levels [8]. Also,

^a Department of the Built Environment, Eindhoven University of Technology, 5612 AP Eindhoven, the Netherlands

^b State Key Laboratory of Silicate Materials for Architectures, Wuhan University of Technology, Wuhan 430070, China

^{*} Correspondence to: Y. Tang and W. Chen, Department of the Built Environment, Eindhoven University of Technology, 5612 AP Eindhoven, the Netherlands; State Key Laboratory of Silicate Materials for Architectures, Wuhan University of Technology, Wuhan 430070, China.

^{**} Correspondence to: K. Schollbach, Department of the Built Environment, Eindhoven University of Technology, 5612 AP Eindhoven, the Netherlands. E-mail addresses: yanjie.tang@polyu.edu.hk (Y. Tang), k.schollbach@tue.nl (K. Schollbach).

variations in cement performance are strongly affected by acidic and alkaline curing environments, which influence strength development. Acidic environments primarily affect early strength (1–3 days), while alkaline environments have a more pronounced effect on the later strength development of cement (7–28 days) [8,9]. Additionally, the induction period of cement hydration is prolonged as pH decreases, and this induction period can be elongated with the simultaneous removal of both calcium and hydroxyl ions, derived from the lower undersaturation degree of alite, and later silicate reaction peak time [10]. Despite extensive research on pH-dependent cement hydration, its role in steel slag activation remains unclear. Unlike cement, steel slag primarily consists of C_2S and $C_2(A,F)$, whose hydration behavior under varying pH conditions is largely unexplored.

The reactions between steel slag and phosphate across a pH range of 4.1 to 12.8 were investigated. In industrial wastewater environments. phosphates do not exist in a single dissolved form but rather as a dynamic equilibrium of H₂PO₄⁻, HPO₄²⁻, and PO₄³⁻ depending on the pH [11]. To replicate this variation, monopotassium phosphate (MKP), dipotassium phosphate (DKP), and tripotassium phosphate (TKP) were used as additives, naturally providing different starting pH and distinct phosphate species upon dissolution. Previous studies used varying amounts of phosphate, complicating the assessment of pH's critical role [2,3,7]. In this study, we standardized the phosphate solution concentration at 0.8 M. Additionally, it is noteworthy that the pH changes in the steel slag system are moderated in case of using phosphate salt buffers. A comprehensive multi-technique approach was employed to elucidate the effects of acidic and alkaline phosphates on hydration kinetics, microstructure, and strength development. This approach included quantitative X-ray diffraction (XRD) analysis, thermogravimetric analysis (TGA), calorimetric measurements, and mercury intrusion porosimetry (MIP), to interpret reaction extent, product identification, heat release, and pore structure. In-situ pH and conductivity measurements, along with ion chromatography (IC) and inductively coupled plasma atomic emission spectroscopy (ICP-OES), were used to analyze earlystage dissolution and precipitation, as well as 28-day leaching behavior. This study provides a deeper understanding of the relationship between phosphate solutions of varying pH and the hydration behavior of steel slag.

A novel strategy for integrating phosphate-rich waste streams into BOF slag activation is thereby presented, offering a sustainable alternative to conventional alkali activators. The insights gained provide a pathway for optimizing phosphate-based activation, advancing the development of durable, low-carbon cementitious materials with industrial scalability.

2. Experiments and methodology

2.1. Raw materials

The basic oxygen furnace (BOF) slag utilized in this study was chosen as the representative steel slag, supplied by Tata Steel in IJmuiden, The Netherlands. The grinding procedure was performed using a Retsch RS 300 XL disc mill at a constant speed of 912 min⁻¹ for 15 min with 1 kg BOF slag grains (0-5.6 mm) in a grinding jar volume of 2 l, and the particle size distribution of the BOF slag powder is given in Fig. 1 and Table 1. The XRD diffractogram of the used BOF slag is shown in Fig. 2, and its chemical, mineralogical composition and other physical parameters are summarized in Table 1. Notably, a negative LOI value refers to the net mass increase observed during calcination of BOF slag prior to XRF analysis, conducted at 1000 $^{\circ}\text{C}$ for 5 h. This increase results from the oxidation of FeO to Fe2O3 over the decomposition of hydroxides and carbonates. Monopotassium phosphate (MKP, KH2PO4), dipotassium phosphate (DKP, K2HPO4) and tripotassium phosphate (TKP, K₃PO₄) were selected as the additives, sourced as a commercially available technical-grade product (VWR Chemicals BDH \mathbb{R} , purity \geq 99.0 wt% analytical reagent).

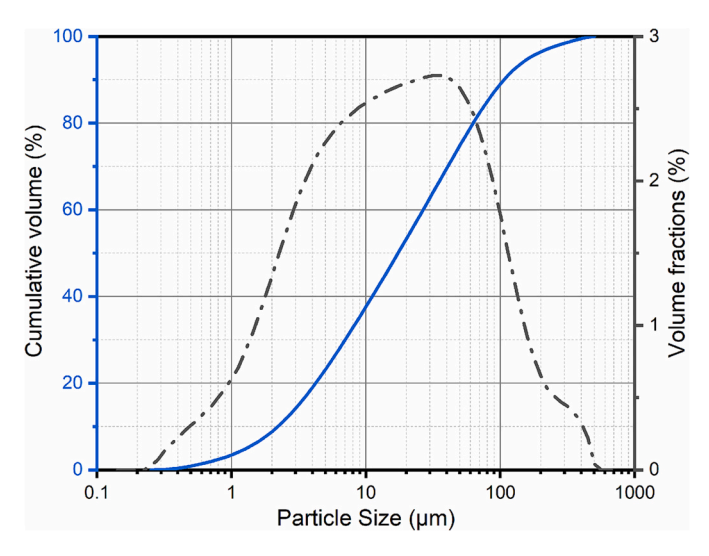


Fig. 1. Particle size distribution of BOF slag.

Table 1Chemical, mineralogical composition and other physical properties of BOF slag.

| Oxide | Content [wt %] ^a | Mineral | Content [wt %] ^b | Physical properties |
|-----------|-----------------------------|----------------|-----------------------------|---------------------------------------|
| MgO | 6.8 | Brownmillerite | 17.1 | $D(0.1)^c=2.22~\mu m$ |
| SiO_2 | 13.45 | Magnetite | 6.4 | $D(0.5)^c = 17.34$ µm |
| Al_2O_3 | 2.21 | C_2S | 39.6 | $D(0.9)^{c} = 106.77$ µm |
| CaO | 40.14 | Wuestite | 20.5 | $\rho^{\rm d} = 3.66 \; {\rm g/cm^3}$ |
| P_2O_5 | 1.61 | Lime | 0.9 | $SSA_{BET}^e = 1.1 \text{ m}^2/$ |
| TiO_2 | 1.39 | Calcite | 0.8 | |
| V_2O_5 | 1.05 | Portlandite | 0.7 | |
| Cr_2O_3 | 0.3 | Amorphous | 14.0 | |
| MnO | 4.61 | Rwp | 2.8 | |
| Fe_2O_3 | 28.32 | | | |
| Others | 0.12 | | | |
| LOI^f | -1.31 | | | |

 $^{^{\}rm a}$ Tested via X-ray fluorescence (XRF, Model Axios Advanced, PANalytical. ${\rm B\cdot V}).$

2.2. Mix design

Based on our preliminary research, the concentrations of phosphate solutions were fixed as 0.8 M. The ratios of volume of phosphate solutions to mass of BOF slag were set as 0.2. The detailed mix proportions of the pastes are shown in Table 2, where the added amounts of water and phosphate solutions are recalculated to mass-based values. The volumes of phosphate solutions were measured by pipette to ensure the constant phosphate molarities in each mixture. The mix proportions containing two types of phosphate solutions were designed to create a pH gradient. MKP, DKP, and TKP solutions inherently provide three distinct pH values. To expand the study, two additional pH levels were introduced by blending MKP with DKP and DKP with TKP, naturally forming intermediate pH values without requiring external acidic or alkaline additives. The varying initial pH values from 4.1 to 12.8 of the phosphate solutions were obtained via the combination of MKP, DKP and TKP solutions. The freshly mixed BOF slag pastes were poured into molds (20 \times 20 \times 20 mm³) and covered with plastic film before demolding. The

^b Quantitative X-ray diffraction (QXRD) analysis via Rietveld method.

 $^{^{\}rm c}$ Analyzed with a laser particle size analyser (Model Malvern Mastersizer 2000, Malvern PANalytical).

^d Particle specific gravity from He pycnometer.

^e Specific surface area determined by Brunauer-Emmett-Teller (BET) method.

f LOI: loss on ignition.

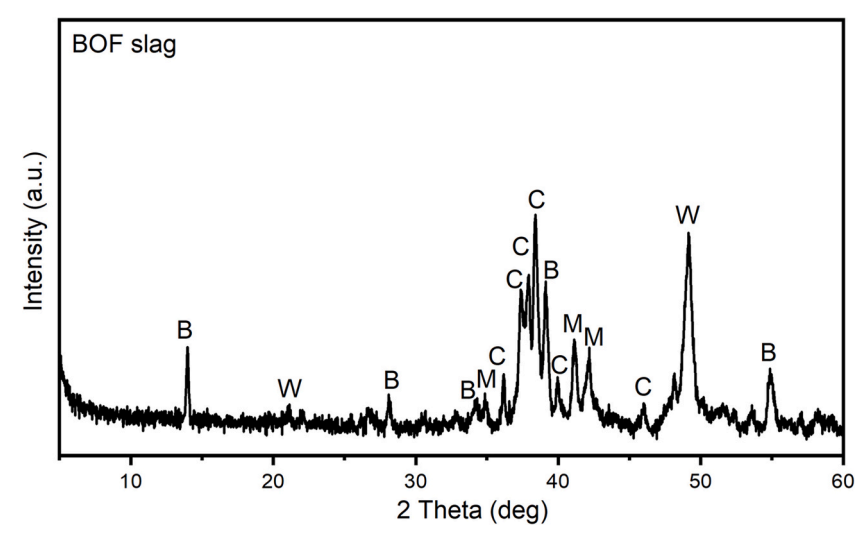


Fig. 2. Phase identification of BOF slag (Legend: B-Brownmillerite, C-C₂S, M-Magnetite, W-Wuestite).

Table 2
Mix proportions.

| | Sample ID | BOF slag | Water | MKP solution | DKP solution | TKP solution | Initial pH | Initial conductivity [mS/cm] |
|--|--------------|-------------|-------|-----------------|-----------------|-----------------|---------------|------------------------------|
| | | [g] | [g] | | | | - | |
| Pastes mixture | REF | 100.0 | 20.0 | | | | 7.0 | / |
| | M | 100.0 | | 21.4 | | | 4.1 | / |
| | MD | 100.0 | | 10.7 | 11.1 | | 6.5 | / |
| | D | 100.0 | | | 22.2 | | 8.8 | / |
| | DT | 100.0 | | | 11.1 | 11.4 | 11.5 | / |
| | T | 100.0 | | | | 22.9 | 12.8 | / |
| Suspension mixture for in-situ pH and conductivity | REF* | 50.0 | 100.0 | | | | 7.0 | 0 |
| measurements | M* | 50.0 | | 107.1 | | | 4.1 | 50.9 |
| | D* | 50.0 | | | 110.8 | | 8.8 | 98.9 |
| | T* | 50.0 | | | | 114.3 | 12.8 | 138.4 |

pastes were air-cured at ambient temperature until the testing age.

To study the early-stage dissolution of BOF slag, in-situ pH and conductivity measurements were performed. An excess of solution with a liquid-volume to slag-mass ratio of 2 was added to ensure full contact of the probes with the liquid. Detailed mix proportions and initial conductivities of phosphate solutions with varying pH are provided in Table 2, where the added amounts of water and phosphate solutions are recalculated to mass-based values.

2.3. Methodology

The hydration heat was recorded using an isothermal conduction calorimeter (TAM Air, Thermometric) from 45 min to 28 days. BOF slag powders were mixed with distilled water or 0.8 M phosphate solutions inside the ampoule for 1 min using a handheld mixer with a stirring tip. The samples were immediately placed in the calorimeter after mixing. The compressive strengths at 7 and 28 days were tested in an MTS Criterion equipped with a load cell of 100 kN at a speed of 0.6 mm/min until collapse according to EN 196–1, with three replicates for each composition.

After the designated curing time, the pastes were crushed and sieved to particles smaller than 2 mm, then immersed in isopropanol for 48 h to stop hydration. The pieces were subsequently dried in a vacuum oven at 45 °C until a constant mass was achieved [12]. After drying, some pieces were finely ground to pass through a 63 μm sieve. The resulting powder and the remaining pieces were stored in desiccators with calcium chloride pellets as a drying agent and sodium hydroxide pellets as a CO2 trap until further testing. The crystalline phases of the hydrated slag

pastes were identified using a Bruker D2 X-ray Diffractometer with a LynxEye detector and a Co X-ray tube, set at 30 kV and 10 mA. The scans were performed over a range of 5 to 80°2θ with a step size of 0.019° and a counting time of 1 s/step. For quantitative phase analysis via the Rietveld method, the counting time was increased to 2 s/step. Si powder (Siltronix, France) was used as an internal standard, making up 10 wt% of the samples. To ensure homogeneity, the samples were mixed thoroughly with the Si powder using an XRD-Mill McCrone (RETSCH) at 75 % speed for 5 min. The TOPAS 5.2 software from Bruker Corporation was utilized to quantify both crystalline and amorphous phases. Thermogravimetric analyses (TGA) were performed with NETZSCH STA 449 F1 instruments. Ground powder samples, each weighing between 30 and 40 mg, underwent heating at a rate of 10 °C/min in a nitrogen atmosphere, covering temperatures from 40 to 1000 °C. The weight loss between 105 and 600 °C is equivalent to the amount of chemically bound water of C-S-H, hydrogarnet, LDHs, portlandite etc. Therefore, the quantification of the amount of chemically bound water excluding portlandite provides an estimate of the total quantity of the other hydration products, as performed according to [12,13]:

$$W_{\textit{Chemically bound water}} = \left(Water loss_{105-600^{\circ}C} - Water loss_{\textit{OH group in Ca(OH)}_{2}}\right) \times 100\%$$
(1)

where *Water loss*_{105-600°C} corresponds to the weight loss from 105 to 600 °C in the total mass fraction, *Water loss*_{OH group} in $_{Ca(OH)_2}$ corresponds to the weight loss from approximately 400 to 500 °C in the total mass fraction.

28-day hydrated BOF slag paste samples were crushed and sieved to particles smaller than 2 mm. Hydration was stopped by immersing the

particles in isopropanol for 48 h, followed by drying in a vacuum oven at 45 $^{\circ}$ C until constant mass was achieved. Particles below 2 mm were selected for porosity analysis, which were obtained by Mercury Intrusion Porosimetry (MIP) measurements using the AutoPore IV 9500 Micromeritics Series Mercury Porosimeter with the maximum pressure of 227.53 MPa. The average pore size was calculated as the volume-weighted mean diameter from mercury intrusion data, using the Washburn equation with a contact angle of 130 $^{\circ}$ and surface tension of 485 mN/m [14,15].

Scanning electron microscopy (SEM) measurements, coupled with energy-dispersive X-ray spectroscopy (EDX) analyses, were conducted on the pastes after 28 days of hydration. The samples were vacuum-impregnation with epoxy-resin, polished, and coated with a thin layer of carbon. The SEM data, specifically the spectral imaging (SI) data, was acquired using a JEOL JSM-7001F SEM equipped with two 170 mm² Ultim Max SDD detectors and AZtec 6.0 software, both from Oxford Instruments. A focused probe with a beam current of 10 nA and an accelerating voltage of 15 kV was employed for the analyses. The PhAse Recognition and Characterization (PARC) software was employed to determine the chemical composition and phase distribution of both the original slag phases and the hydration products. A comprehensive description of the PARC technique can be found elsewhere [16].

The leaching test of 28-day cured slag pastes was conducted according to EN 12457–2, a one-stage batch leaching test [17]. Deionized water was added to the crushed samples (below 4 mm in size) at a liquid-to-solid ratio of 10, and the mixture was agitated using a dynamic shaker (ES SM-30, Edmund Buhler GmbH) for 24 h. After shaking, the leachates were filtered through a 0.22 μm syringe filter. The pH of the filtrates was measured using a Greisinger-GMH 5500 pH meter, with three readings taken and averaged for each sample. Liquid samples were either used undiluted or diluted by a factor of 10 for further elemental concentration analysis. The ion concentrations were determined using a Thermo Scientific Dionex ICS-1100 ion chromatography (IC) system or an inductively coupled plasma atomic emission spectrometer (ICP-OES, SPECTROBLUE) after acidification with concentrated HNO3.

To study the early-stage dissolution of BOF slag, in-situ pH and conductivity measurements were performed using a handheld conductivity meter (Greisinger-GMH 3431) and a pH meter (Greisinger-GMH 5500). The experiments were conducted in a climate-controlled room maintained at $20\pm0.5\,^{\circ}\text{C}$ and 60 % relative humidity. The probes were first immersed in distilled water or phosphate solutions until temperature, pH, and conductivity stabilization was achieved. BOF slag powder was then added to the liquid media and stirred for 30 s using a handheld mixer. Data logging was set at 1-min intervals for a 90-min duration. To prevent evaporation, the beaker used for measurements was sealed with parafilm and tape.

Ion concentrations at 10 and 90 min were measured. Due to the strong buffering effects of the phosphate, samples with phosphate solutions were not acidified but were diluted by factors of 10 or 100. Solids were separated by filtration and immersed in isopropanol for 2 h to stop hydration. The isopropanol was then removed, and the solids were dried in a vacuum oven at 45 $^{\circ}\mathrm{C}$ until a constant mass was achieved. The dried samples were subsequently used for XRD analysis.

3. Results and discussion

3.1. Early-stage dissolution and precipitation

Due to the low water-to-solid (w/s) ratio, in-situ measurements of pH and conductivity are technically challenging. Therefore, a mixture of phosphate solution and BOF slag with a volume-to-slag mass ratio of 2 was used. Although this method significantly increases the phosphate amount, it closely simulates the early-stage dissolution of BOF slag under low w/s conditions, providing insights into pH evolution and ion concentration changes.

Upon mixing, REF* exhibits an immediate increase in conductivity

and pH (Fig. 3). This increase can be attributed to the incongruent dissolution of C_2S and brownmillerite, as shown in Fig. 4 that Ca shows a concentration of around 20 mmol/l and the concentrations of other elements (Fe, Al and Si) are at best around 0.01 mmol/l. The temperature in REF* remains stable, indicating the limited reactivity of BOF slag with water. At around 10 min, a slight pH increase is observed, stabilizing shortly after, along with a slight increase in Si concentration at 90 min, due to the further dissolution of C_2S . The decline in conductivity corresponds with a decrease in Al, Fe, and Mg concentrations, indicating the formation of pyroaurite (Fig. 5).

In mixtures containing phosphate, a significant decrease in conductivity is noted due to the rapid precipitation of various phosphate compounds, as phosphate ions interact with iron, aluminum, magnesium, and calcium across a wide pH range [18]. Unlike M* and D*, T* starts increasing conductivity at around 10 min, indicating that dissolution is predominant instead of precipitation. In M*, a dramatic temperature rise of $\Delta T \approx 7$ °C occurs, due to acid-base reactions between with a strong exothermic response [19]. Dissolution at alkaline conditions, as seen in D* and T* (Fig. 3), is more gradual. Phosphate addition enhances the dissolution of Al, Fe, and Si, which is more pronounced at higher pH levels. Variations in Ca and Mg concentrations are controlled by the saturation of different calcium and magnesium phosphate phases at specific pH levels, as the stabilized pH ranges of M*, D*, and T* vary due to the buffering effects of different amounts of $H_2PO_4^-$, HPO_4^{2-} , and PO₄³⁻ ions [20]. The resulting precipitates differ with pH, including brushite (CaHPO₄·2H₂O) at ~8.4, montgomeryite (Al₄Ca₄Mg $(PO_4)_6(OH)_4 \cdot 12H_2O)$ at ~10.6, and vauxite $(FeAl_2(PO_4)_2(OH)_2 \cdot 6H_2O)$ and bobierrite (Mg₃(PO₄)₂·8H₂O) at \sim 13.0, as shown in Fig. 5. Vauxite disappears at 90 min, likely converting into hydroxyapatite, a phase with higher thermodynamic stability at high pH [21,22]. These different formed phases indicate how phosphate reacts with various ions across a broad pH range. However, these reactions may not occur in BOF slag under low w/s conditions due to much lower phosphate content, or they may occur extremely rapidly upon mixing when the water to solid ratio still comprises only the surface of the slag particles and effectively is much higher.

3.2. Hydration

3.2.1. Kinetics

The results of isothermal conduction calorimetry are depicted in Fig. 6. A minor peak is evident at approximately 2 days for REF, with the cumulative hydration heat reaching 37.6 J/g at this time, which is more than 50 % of the total heat release (62.3 J/g) at 28 days. After this initial peak, the increase in hydration heat for REF is slow. The exothermic reaction of brownmillerite hydration typically occurs within the first several hours [23,24]. Brownmillerite dissolves rapidly upon contact with water, forming a metastable C-(A,F)-H gel that coats the surface of brownmillerite. This gel coating retards further hydration of brownmillerite, although it eventually converts to stable hydrogarnet [23,24]. Additionally, the C-(A,F)-H gel in REF can be iron-rich and less soluble due to the higher iron content of brownmillerite in BOF slag compared to that in cement clinker [23-25]. These factors explain the delayed exothermic peak in REF. C2S has a low reactivity, leading to its complete hydration taking several weeks or even months [26]. The prolonged hydration of C2S can contribute to the slow accumulation of heat at later stages.

The introduction of phosphate solutions significantly elevates the hydration heat at 28 days in all samples except M. M starts accelerating its reaction after 3 weeks, as shown in Fig. 6, and it is expected to generate a higher heat release than REF at higher ages. The initial low pH (4.1) may restrict the hydration of brownmillerite and facilitate the fast dissolution of C_2S initially, but this is not recorded in the heat release. The buffering regime of $H_2PO_4^-$ and HPO_4^{2-} in maintains a pH range of 7–7.5, increasing the saturation level of hydration products like C-S-H and hydrogarnet and thereby hindering the further dissolution

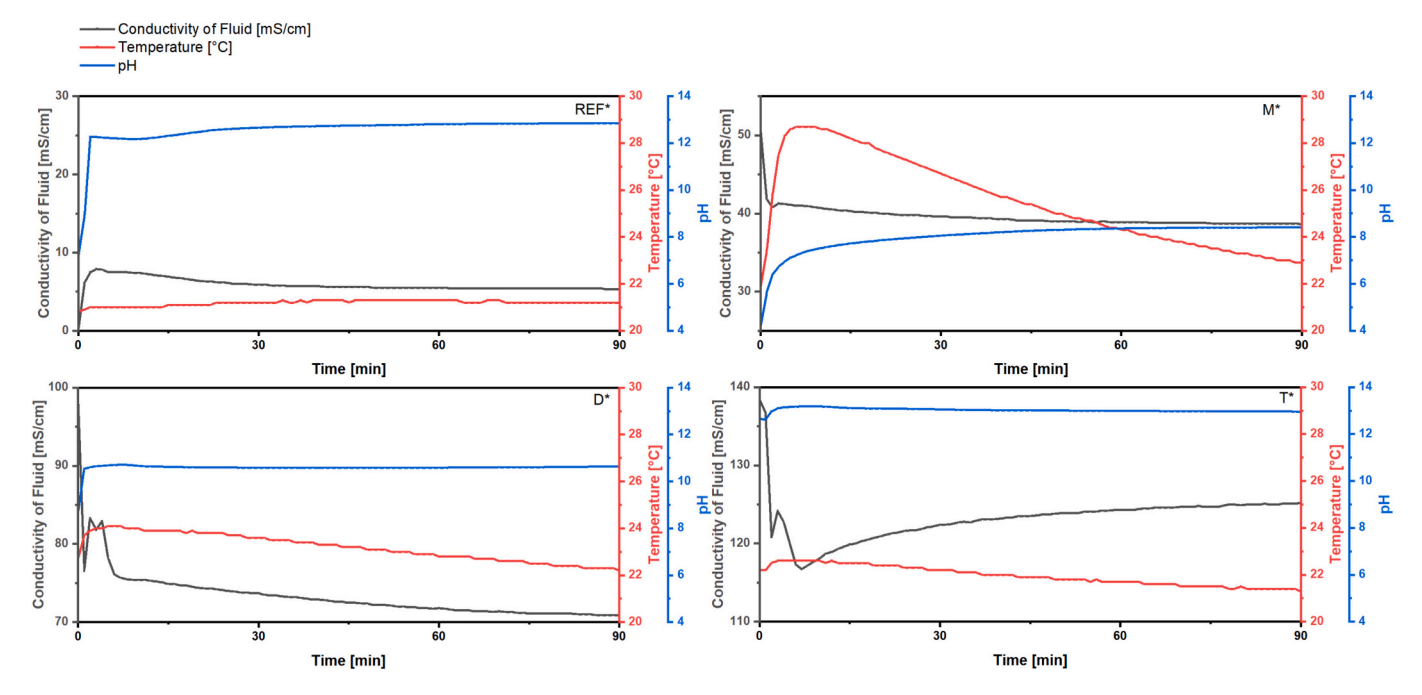


Fig. 3. The in-situ pH and conductivity of different suspension mixtures.

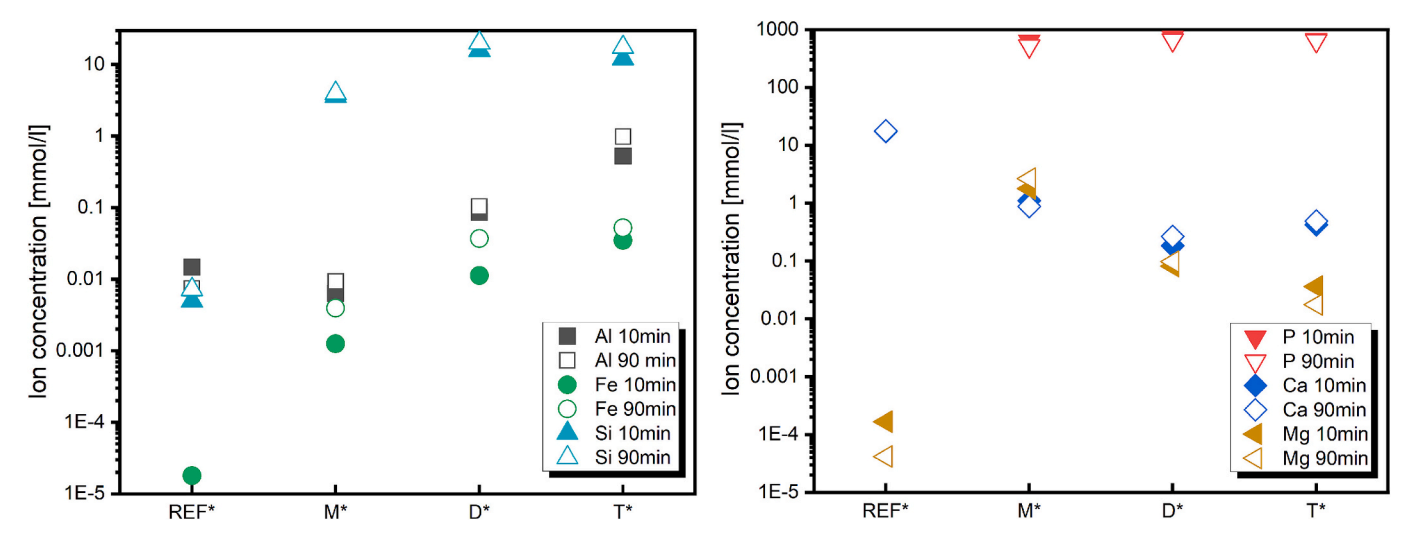


Fig. 4. Ion concentration changing of different suspension mixtures.

and precipitation [20,27]. This buffering role occurs in all samples whereas the buffered pH increases with the higher alkaline phosphate input. Consequently, the retardation effects diminish with increasing initial pH. T shows the highest hydraulic reactivity, with the main exothermic reaction completing within 3 days and a 28-day cumulative heat of approximately 145 J/g. High pH favours the dissolution of ironcontaining phases, such as the original brownmillerite and the initially formed C-(A,F)-H gel and hydroferrite [28,29]. MD, D, DT, and T exhibit comparable overall hydration heat at 28 days, indicating that equal phosphate input can result in similar hydration extent once the buffering barrier of $\rm H_2PO_4^-/HPO_4^2-$ is overcome.

3.2.2. Hydration products identification via XRD

Fig. 7 illustrates the phase composition of 7- and 28-day hydrated BOF slag pastes. Generally, hydrogarnet, pyroaurite, and hydrotalcite are the main crystalline hydration products, as detected via XRD. Hydrogarnet $(Ca_3(Al_xFe_{1-x})_2(OH)_{12})$ is a typical hydration product of brownmillerite in the absence of other phases like gypsum [23].

Notably, brownmillerite also apparently hydrates with consumption of some C2S to produce siliceous hydrogarnets covered by the general formula $Ca_3(Al_xFe_{1-x})_2(SiO_4)_y(OH)_{4(3-y)}$, where the Al/Fe ratio is unknown [30]. The diffraction peak of hydroxy-AFm (OH-AFm, mainly Ca₄Al₂O₇·19H₂O) is detected but with low intensity. This metastable phase, originating from brownmillerite, can gradually convert into hydrogarnet and portlandite over time [31-33]. The presence of hydroxy-AFm in some samples (D, DT, T) at 28 days might be due to the initial high pH and promoted brownmillerite hydration, as T also shows the peak of hydroxy-AFm at 7 days. The detection of pyroaurite and hydrotalcite, which are LDHs and can be represented by the general formula Mg₃(Al,Fe)(OH)₈(CO₃)_{0.5}·2H₂O, indicates the hydration of wuestite since the release of magnesium is controlled by wuestite dissolution [34]. The precipitation of hydroxyapatite was expected but this phase can be present in small amounts with poor crystallinity [21,35], making hydroxyapatite invisible in XRD.

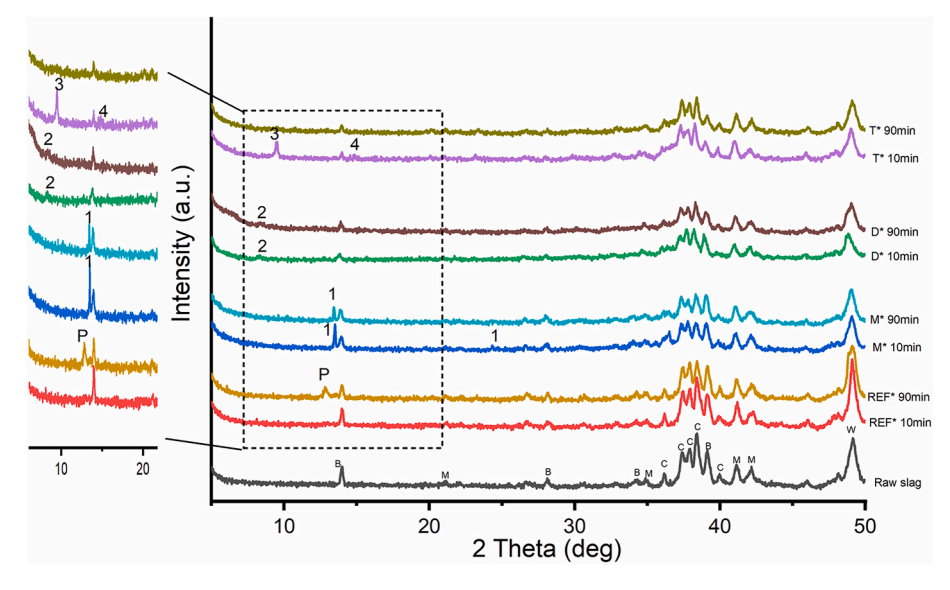


Fig. 5. XRD data of BOF slag suspensions with different solutions (Legend: 1-Brushite, 2-Montgomeryite, 3-Vauxite, 4-Bobierrite, P-Pyroaurite, B-Brownmillerite, C-C₂S, M-Magnetite, W-Wuestite).

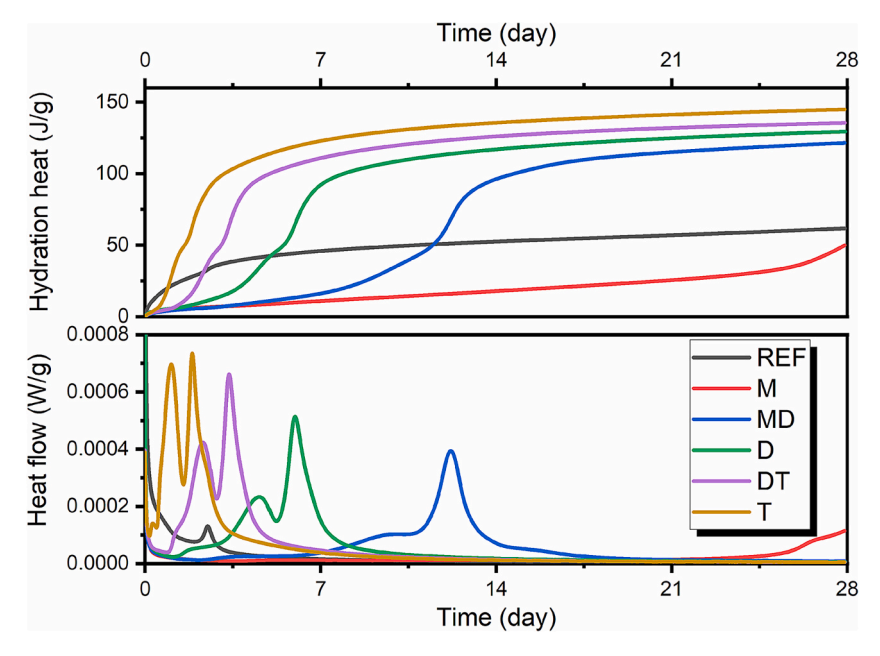


Fig. 6. Heat flow and cumulative heat evolution of BOF slag pastes.

3.2.3. Phase evolution

Further insights into the phase evolution at different initial pH values are drawn from the quantification of 1-, 7- and 28-day hydrated BOF slag pastes using XRD Rietveld analysis, as presented in Fig. 8. The decline of brownmillerite at 1 day in REF leads to a modest increase in hydrogarnet and LDHs (pyroaurite and hydrotalcite) [34,36]. C_2S begins to react after 1 day, showing only a minor decline. The absence of portlandite further evidences the limited hydration of C_2S at 1 day. At 7 days, the consumption of C_2S and brownmillerite remains unchanged, indicating the slow hydration process of BOF slag with water. At 28 days, both C_2S and brownmillerite in REF show continuous hydration, with C_2S decreasing to a larger extent, contributing to the increasing amorphous phase content.

It is evident that phosphate addition accelerates the reaction of C_2S . At 1 day, the reaction extent of C_2S in M and MD is more pronounced compared to that in samples with alkaline phosphate solutions,

alongside the formation of more amorphous phases including possible calcium phosphate compounds such as brushite and octacalcium phosphate, which form at pH levels below 7 [37,38]. The decline in C_2S at 1 day is not consistent with the heat release shown in Fig. 6, indicating that the consumption of C_2S is probably caused by the immediate dissolution post-mixing due to the acidic nature of M rather than hydration. Additionally, the acidic environment does not benefit the reaction of brownmillerite at 1 day. Notably, D shows the least hydration extent of both C_2S and brownmillerite in all samples and this extent increases with higher pH in samples D, DT, and T, correlating well with the increase in hydration products.

At 7 and 28 days, the consumption of C_2S and brownmillerite shows a generally clear trend that higher initial pH leads to greater hydration. For M, the added phosphate still shows limited effects on the brownmillerite hydration at 7 days but significant decrease in brownmillerite is observed at 28 days. In MD, the noticeable decline in C_2S and

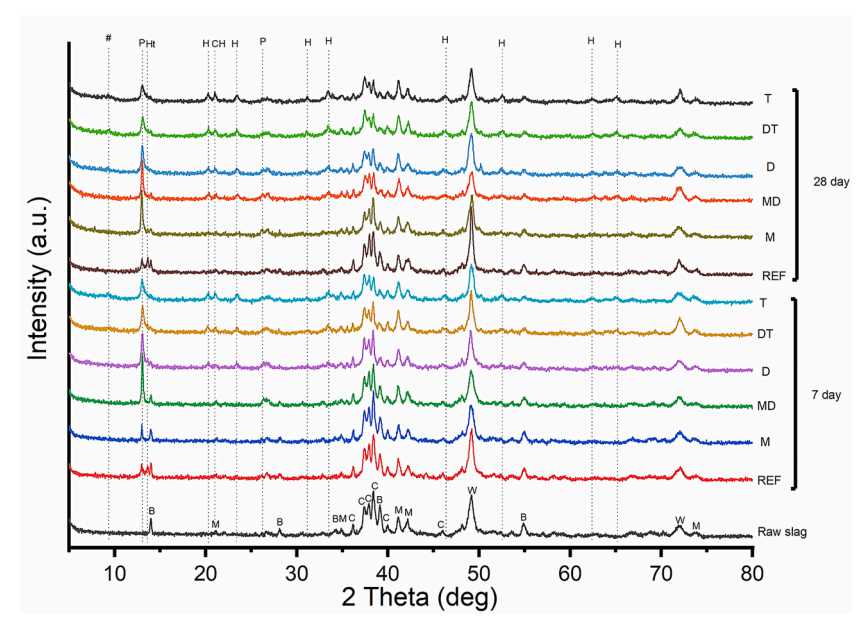


Fig. 7. Phase identification of 7- and 28-day hydrated samples (Legend: # -Hydroxy-AFm, P-Pyroaurite, Ht-Hydrotalcite, H-Hydrogarnet, CH-Portlandite, B-Brownmillerite, C-C₂S, M-Magnetite, W-Wuestite).

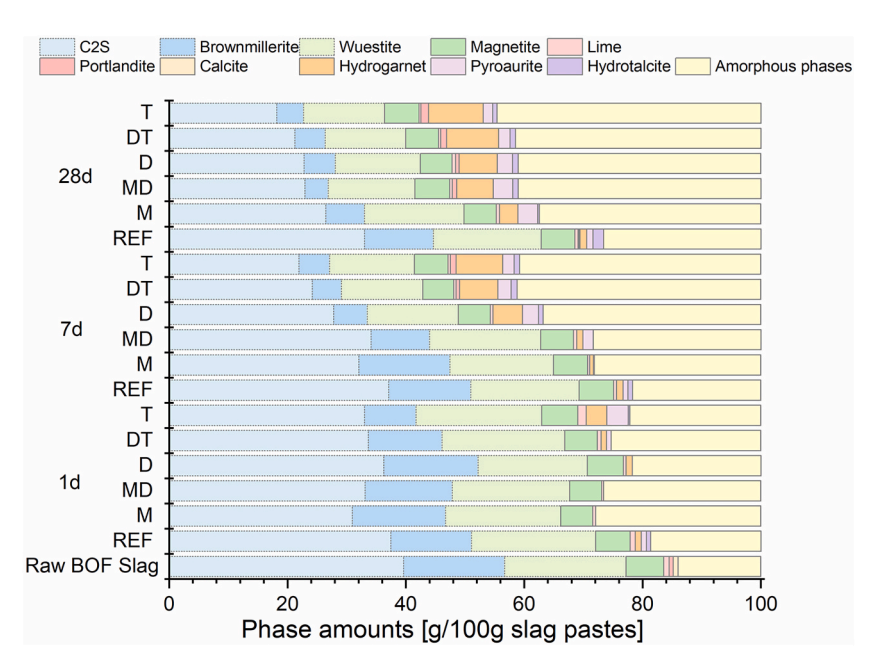


Fig. 8. QXRD results of 1-, 7- and 28-day hydrated BOF slag pastes (Hydroxy-AFm is included in the amorphous phases due to its low content in hydration products and low crystallinity).

brownmillerite does not correspond to a proportional increase in hydrogarnet and LDHs at 7 days. The primary hydration of MD completes after about 2 weeks, as indicated in Fig. 6. Therefore, it can be assumed that the decline in C₂S and brownmillerite in MD at 7 days promotes the initial formation of metastable phases with poor crystallinity, which gradually convert to stable hydrogarnet and LDHs, releasing heat in the process. The other samples D, DT, and T exhibit high degrees of hydration at 7 days, along with considerable amounts of hydration products. The highest amount of portlandite is detected in T at both 7 and 28 days, attributed to the significantly promoted hydration of C₂S. Additionally, C₂S can prompt a series of secondary reactions with brownmillerite to produce straetlingite, siliceous hydrogarnets, and C-S-H, consuming portlandite in the process [39,40]. Magnetite remains relatively stable, while wuestite exhibits a notable decrease at 7 days in

the presence of phosphate solutions with initial pH above 7. Pyroaurite is detected in greater amounts than hydrotalcite in all phosphate-containing samples, reflecting the iron-rich nature of the BOF slag system. This also indicates that phosphate may preferentially stabilize ${\rm Fe}^{3+}\text{-rich}$ LDHs like pyroaurite by forming Fe-phosphate complexes, hindering hydrotalcite crystallization.

3.2.4. Reacted phases and hydration heat

Fig. 9 illustrates the amounts of reacted C_2S , brownmillerite, and wuestite in 28-day hydrated BOF slag pastes with phosphate solutions at different initial pH values. The reaction amounts of these phases are normalized for water loss at 600 °C. Although the initial low pH in some samples retards hydration, the addition of phosphate ultimately leads to significantly more reacted phases compared to REF at 28 days. Higher

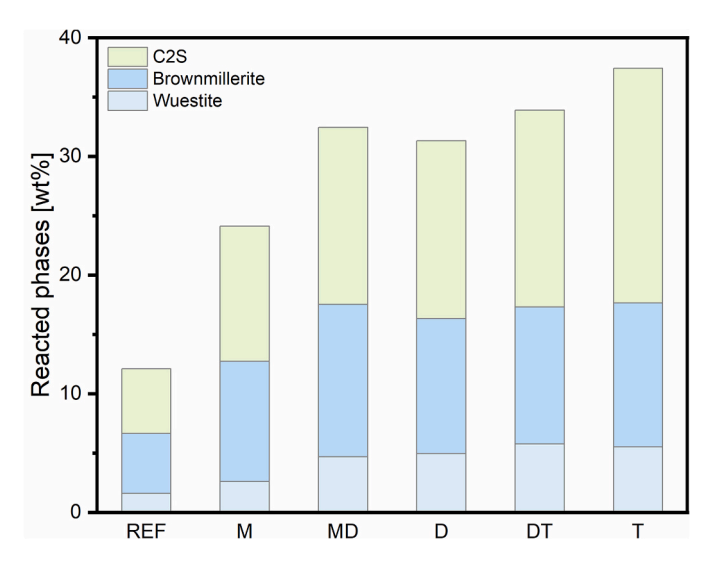


Fig. 9. Amounts of reacted C_2S , brownmillerite and wuestite at 28 days with indicated phosphate salt buffer as pH-proxy.

initial pH enhances the reaction extent, with C_2S comprising the largest proportion of reacted phases. Brownmillerite shows a relatively higher reaction extent than C_2S , as its original amount is approximately half that of C_2S , as indicated in Table 1. Despite variations in pH affecting the reaction extent of C_2S , brownmillerite, and wuestite, the total hydration extent is more or less comparable for all samples containing phosphate, except for M.

Different clinker phases generate varying amounts of heat upon hydration. Based on the consumption of original phases in BOF slag pastes shown in Fig. 9, the overall hydration heat at 28 days can be calculated. This allows for verification of the contributions from the dissolution and precipitation processes of specific phases in BOF slag to the overall heat release during hydration. The hydration of BOF slag involves multiple overlapping precipitation reactions that occur after dissolution. These precipitation reactions are difficult to study in isolation because they occur simultaneously and progressively as hydration advances. Besides, despite that the overall heat effect incorporates both dissolution and precipitation, the heat effect can be more allocated to the dissolution reaction depending on the thermodynamic data used, and dissolution of the clinker phases can be assumed to be the dominant heat contributing reaction [41]. Consequently, a simplified approach has been applied that dissolution enthalpy is used to represent the reaction enthalpy [41]. The dissolution reactions of brownmillerite and C₂S are represented by [42,43]:

$$\begin{aligned} \text{Ca}_2\text{Fe}_2\text{O}_5 + 5\text{H}_2\text{O} &\rightarrow 2\text{Ca}^{2^+} + 4\text{OH}^- + 2\text{Fe}(\text{OH})_{3(\text{am})} \ \Delta\text{H}_{R(\text{Ca}2\text{Fe}2\text{O}5)} \\ &= -428.76 \ [\text{J/g}] \end{aligned} \tag{2}$$

$$\label{eq:ca2SiO4} \begin{split} \text{Ca}_2 \text{SiO}_4 + \text{H}_2 \text{O} \rightarrow 2 \text{Ca}^{2+} + 2 \text{OH}^- + \text{SiO}_3{}^{2-} \ \Delta \text{H}_{\text{R(Ca2SiO4)}} = \ -298.95 \ [\text{J/g}] \end{split} \tag{3}$$

The hydration of wuestite releases certain amounts of Mg, Mn, and Fe, with Mg contributing more significantly than Mn and Fe to the formation of LDHs [34,44]. Consequently, the reaction of wuestite can be simplified by considering MgO as the primary reacted phase, assuming the dissolution of Fe^{2+} and Mn^{2+} is minor. The reaction of wuestite is described using the simplified equation:

$$MgO + H_2O {\to} Mg^{2+} + 2OH^- \Delta H_{R(MgO)} = -959.25 \ [J/g] \eqno(4)$$

The reaction enthalpies of C_2S , brownmillerite, and wuestite are determined using the thermodynamic data listed in Table 3. The overall heat release, calculated based on the amounts of reacted phases in the 28-day hydrated BOF slag pastes, is determined with the equation:

Table 3Enthalpies of each phase/species used for the calculation of the overall heat release.

| Phases/species | $\Delta H_{\rm f}$ [kJ/mol] | Reference | |
|--|-----------------------------|-----------|--|
| Ca ₂ Fe ₂ O ₅ | -2124.22 | [43] | |
| Ca ₂ SiO ₄ | -2307.6 | [45] | |
| MgO | -601.70 | [46] | |
| H ₂ O | -285.88 | [47] | |
| Ca ²⁺ | -543.07 | [47] | |
| OH- | -230.01 | [47] | |
| Fe(OH)3(am) | -832 | [43] | |
| SiO ₃ ²⁻ | -1098.74 | [47] | |
| Mg ²⁺ | -465.93 | [46] | |

$$Q_{sum} = (\Delta H_{R(Ca2SiO4)} \times W_{R(Ca2SiO4)} + \Delta H_{R(Ca2Fe2O5)} \times W_{R(Ca2Fe2O5)}$$

$$+ \Delta H_{R(MgO)} \times W_{R(MgO)}) \times M_{Input}$$
(5)

where Q_{sum} [J] is the total theoretical heat release, $\Delta H_{R(i)}$ [J/g] is the reaction enthalpy of phase i, $W_{R(i)}$ [wt%] is the reacted amount of phase i at 28 days (derived from QXRD, as shown in Fig. 9), and M_{Input} [g] is the BOF slag mass used in the calorimetry test.

This theoretical heat is compared with the measured heat via calorimetry, as shown in Fig. 10. The small deviation between the calculated and measured heat release in MD, D, DT, and T indicates the completed hydration of the reacted phases reached equilibrium, with the contribution of wuestite to the overall exothermic reaction being as comparable as that of C₂S and brownmillerite. The measured heat higher than the calculated heat in REF can be attributed to the hydration of other original phases not included in the calculation. This exclusion of other hydrated original phases happens in all samples and affects more apparently the obtained value for REF. However, a large disparity is observed in M, where the calculated heat is much higher than the measured heat. This demonstrates that with acidic phosphate the hydration of BOF slag occurs differently from alkaline phosphate, initiating with an acid-base reaction where dissolution due to its acidic nature proceeds immediately upon mixing. This rapid dissolution concludes within the first 45 min, and thus, the corresponding heat release is omitted by the calorimeter measurement. Additionally, the reaction enthalpy is calculated based on the complete hydration. Hence, the formation of metastable phases with low heat release in M at 28 days is supported, indicating that the H₂PO₄-/HPO₄²⁻ buffering regime hinders the conversion of these metastable phases into stable hydrogarnet and LDHs, similar to the observation in MD at 7 days.

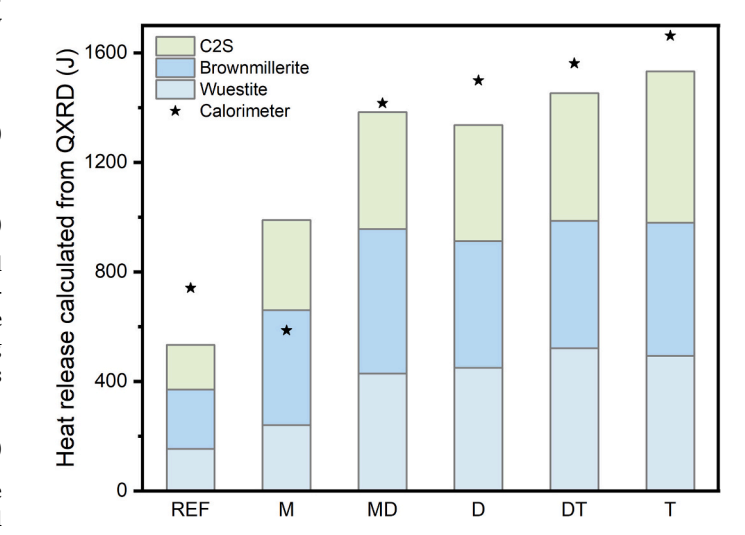


Fig. 10. The comparison between the theoretical heat release calculated based on the amounts of reacted phases and the measured heat from calorimeter of 28-day hydrated BOF slag pastes.

3.2.5. Thermogravimetric analysis

The weight loss of the hydrated BOF slag pastes at various temperature stages is shown in Fig. 11 and Fig. A2. The decomposition of hydrogarnet and other hydration products, particularly X-ray amorphous C-S-H gel, upon heating provides an indication of the overall amount of hydration products [48]. C-S-H exhibits water loss over a wide temperature range from 40 to 600 °C due to the loss of water in the interlayer and dehydroxylation, with the main decomposition peak typically occurring between 40 and 200 °C [12]. Although hydroxyapatite is not detected via XRD, the added phosphate ultimately converts into hydroxyapatite through its reaction with calcium, owing to hydroxyapatite's high thermodynamic stability [49,50]. The removal of adsorbed water in hydroxyapatite at around 105 $^{\circ}\text{C}$ is also noted [21,51], which is lower than the decomposition peak of C-S-H at around 150 °C, as shown in Fig. 11. It is evident that the addition of phosphate promotes the formation of C-S-H gel in all samples except M at 7 days, confirming the retardation effects of acidic phosphate on C₂S hydration.

The dehydration of hydrogarnet and LDHs occurs within the temperature range of 200 to 400 °C. The mass loss of these phases increases with the addition of phosphate at higher initial pH levels, with a continuous rise observed over time. The higher pH also results in a greater amount of portlandite, which decomposes at temperatures between 400 and 500 °C [12], consistent with the QXRD results. In the presence of phosphate, the formation of hydroxyapatite is favored over portlandite [52]. With equal phosphate input, samples D, DT, and T exhibit a more distinct dehydroxylation peak of portlandite compared to REF at 7 days, further demonstrating the accelerating effects of alkaline phosphate on C_2S hydration.

Another weight loss observed from 500 to 720 °C signifies the decomposition of carbonate groups [12]. While the amount of calcite determined via XRD Rietveld method is negligible, this mass loss most likely originates from the carbonate compounds such as amorphous calcium carbonate and the formed LDHs, confirmed by the split carbonate peaks in some samples (DT and T at 7 days) [53]. It should be noted that B-type carbonated hydroxyapatite may form via the substitution of PO_4^{3-} by CO_3^{2-} , showing an overlapping temperature range of decarbonation from 500 to $1000\ ^{\circ}$ C [54,55]. Additionally, a final weight loss range corresponding to the dehydroxylation of hydroxyapatite is observed above 720 °C in phosphate-containing samples [51,56]. However, this mass loss is absent in M and MD at 7 days, likely due to the formation of other metastable phosphate-containing phases like (Al,Fe) PO_4 formed at pH below 7, which can transform into hydroxyapatite as the pH increases over time [22].

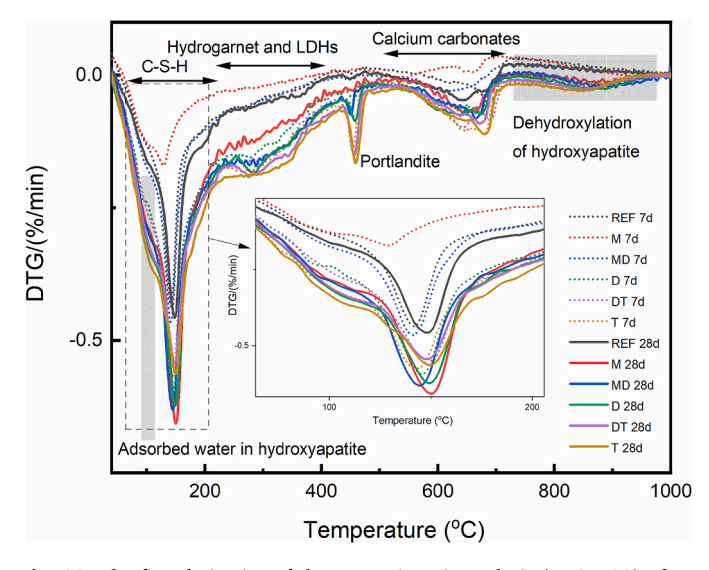


Fig. 11. The first derivative of thermogravimetric analysis (DTG/TGA) of 7- and 28-day hydrated BOF slag pastes.

3.2.6. Chemically bound water and hydration heat

Fig. 12 compares the overall cumulative heat release with the chemically bound water content measured from TGA for 7- and 28-day hydrated BOF slag pastes. The addition of phosphate increases the content of chemically bound water, which correlates with the higher initial pH. One exception is M at 7 days, revealing its limited hydration. Fig. 12 shows that the total hydration heat is directly proportional to the chemically bound water, demonstrating a good correlation with an R² value of 0.86. However, MD at 7 days and M at 28 days deviate from this trend, likely due to the exclusion of the first 45-min heat release and the low heat release associated with the favored formation of metastable phases at low initial pH.

3.2.7. SEM analysis

Additional SEM and EDX analyses have been conducted, as presented in Fig. 13. The backscattered electron (BSE) image reveals a dense microstructure, consistent with enhanced hydration. The crystalline and amorphous hydration products, characterized by submicron particle sizes, are intricately intermixed, hindering the differentiation of individual phases such as C-S-H, hydrogarnet, and others using EDX [16], which has a spatial resolution of approximately 1 μ m. Consequently, these phases are collectively classified as a single hydration product. Similarly, portlandite, calcite, and lime are grouped together due to challenges in distinguishing them via EDX. Likewise, wuestite and magnetite are combined into a single category for the same reason.

Fig. 13 reveals a uniform distribution of phosphorus (P) within the hydration products, suggesting that phosphate ions are finely dispersed, existing as amorphous or nanocrystalline calcium phosphate phases embedded within the matrix. The absence of P enrichment at boundaries around C_2S and brownmillerite indicates that phosphate ions promote slag hydration by facilitating the dissolution of reactive phases (e.g., C_2S and brownmillerite) rather than forming distinct phosphate-rich layers on their surfaces. This aligns with enhanced hydration and improved mechanical performance in this binder system, indicating that phosphates act as homogeneous activators modifying the binder chemistry.

3.3. Porosity and mechanical performance

The pore structure of 28-day hydrated BOF slag pastes was analyzed using MIP measurements, with the results shown in Fig. 14 and Table 4. REF exhibits the highest porosity at 21.2 %, resulting in the lowest strength of 7.7 MPa at 28 days (Fig. 15). The addition of phosphate optimizes the pore structure by significantly reducing capillary porosity. Consequently, all phosphate-containing samples demonstrate a

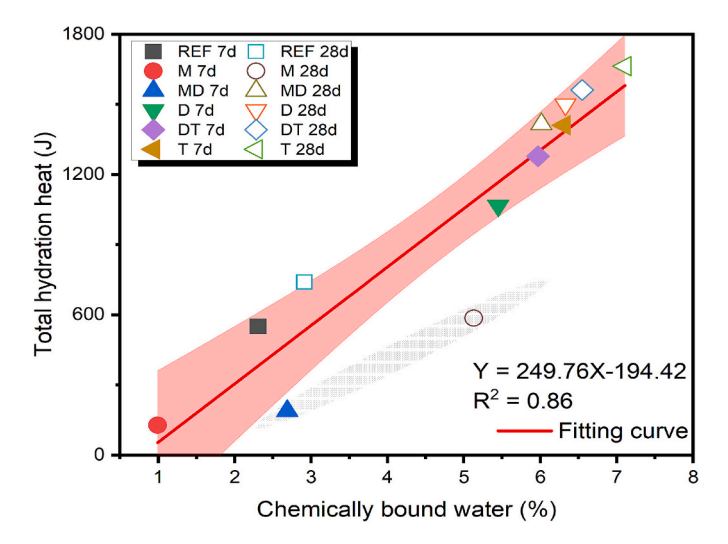


Fig. 12. The correlation between the chemically bound water of 7- and 28-day hydrated BOF slag pastes and its hydration heat and its fitting curve.

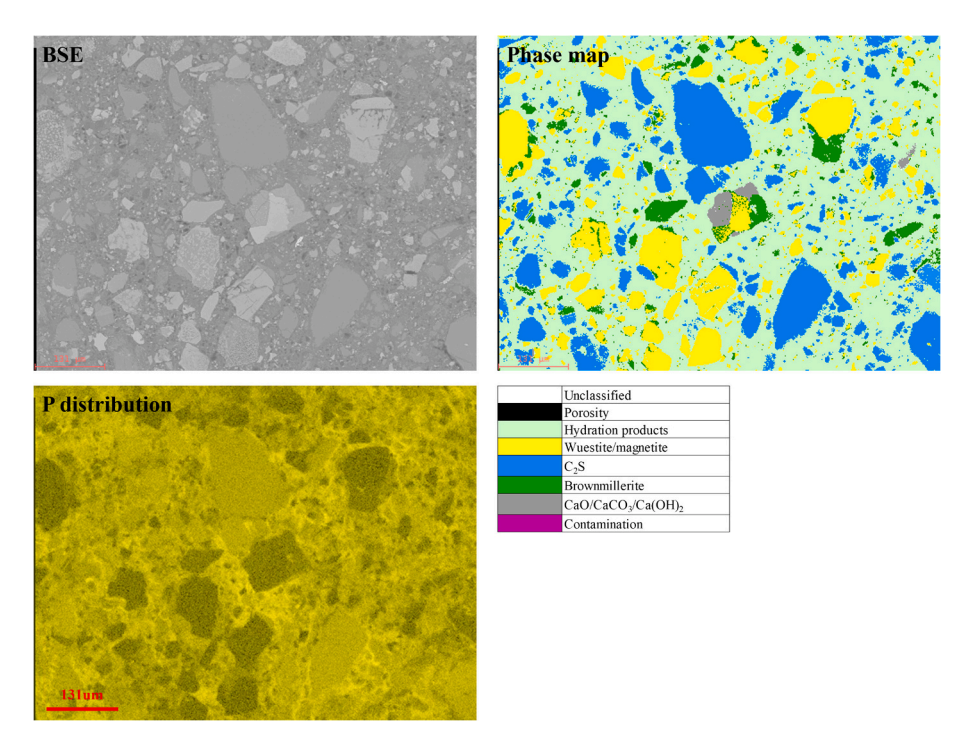


Fig. 13. Representative backscattered electron (BSE) image, PARC phase map and P elemental distribution (in yellow) of sample D after 28-day hydration. (Note: During the steelmaking process, phosphorus is typically oxidized and transferred into the slag, where it is primarily incorporated into C_2S , as identified through PARC analysis.) (For interpretation of the references to colour in this figure legend, the reader is referred to the web version of this article.)

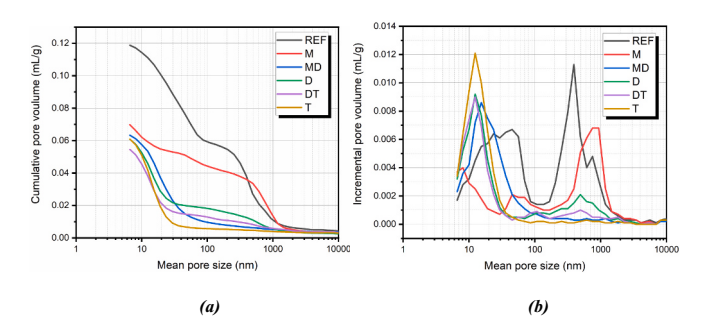


Fig. 14. (a) The cumulative pore volume and **(b)** incremental pore volume of 28-day hydrated BOF slag pastes.

Table 4Porosity and density of 28-day hydrated BOF slag pastes.

| Sample | Porosity [%] | Average pore size [nm] | Bulk density [g/cm ³] | | |
|--------|--------------|------------------------|-----------------------------------|--|--|
| REF | 21.2 | 38.8 | 1.81 | | |
| M | 13.9 | 34.7 | 2.00 | | |
| MD | 13.8 | 13.3 | 2.20 | | |
| D | 13.9 | 17.4 | 2.30 | | |
| DT | 11.9 | 15.5 | 2.20 | | |
| T | 13.2 | 13.6 | 2.17 | | |

reduction in both porosity and average pore size at 28 days, consistent with enhanced hydration. The overall porosities of all phosphate-containing samples are comparable, as well as their workability observed during mixing and molding. However, the strengths of M and DT are significantly different, with 28-day strengths of 37.7 MPa for M and 66.9 MPa for DT. M has a higher proportion of capillary pores (>10 nm) and a larger average pore size of 34.7 nm. The noticeable increase in strength from 7 to 28 days in M is attributed to its retarded hydration during the first 3 weeks. A similar significant increase in strength is observed in MD due to the formation of metastable phases rather than

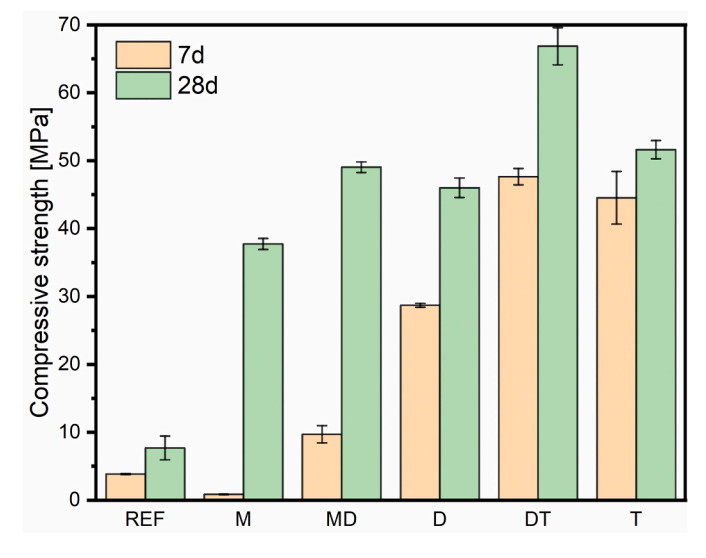


Fig. 15. The strength development of 7- and 28-day hydrated BOF slag pastes.

hydrogarnet and LDHs at 7 days, as explained with Fig. 12. The contradiction between the higher hydration extent and lower strength of T compared to DT is notable. This can be explained by the higher potassium concentration in T, leading to shrinkage during air curing, particularly under low w/s conditions being more sensitive to alkali enrichment [57], consistent with the increased porosity and reduced bulk density of T (13.2 % and 2.17 g/cm³) and compared to DT (11.9 % and 2.20 g/cm³). Overall, while the elevated pH of phosphate solutions enhances the hydration extent of BOF slag pastes, attention should be given to potential shrinkage due to high alkali enrichment to ensure strength development. Further investigation should be conducted regarding the effects of alkalis on the pore structure and strength development in phosphate-activated BOF slag pastes.

3.4. Leaching

The leaching of vanadium (V) and chromium (Cr) is of significant concern, as these are the two most concentrated heavy metals in the BOF slag used in this study, as indicated by the chemical composition (Table 1). V is primarily incorporated into C2S and brownmillerite, while Cr resides in brownmillerite and wuestite [58]. The hydration of C₂S brownmillerite and wuestite can release these heavy metals, while their retention by hydration products like C-S-H gel and hydrogarnet can occur simultaneously [34,59]. This explains the lack of Cr leaching due to the immobilization capacity of the abundant hydration products, despite the significantly promoted hydration of brownmillerite and wuestite in the presence of phosphate. V remains relatively immobile in highly alkaline environments, and its leaching decreases with increasing pH [58,60,61]. A similar observation is noted in Table 5 and Fig. 16. The final pH is slightly higher with the initial higher pH of phosphate input, and while V leaching differences are minimal, they correlate well with the pH trend. Additionally, the final K concentrations are proportional to the initial K input for the phosphate-containing samples. Although C-S-H can adsorb small amounts of K, most K is dissolved during the leaching process [62].

3.5. Mechanism discussion

A certain amount of brownmillerite and C_2S is dissolved initially after mixing, driven by variations in pH and phosphate availability in the pore solution. Subsequently, phosphate compounds form readily, but the reactions differ between acidic and alkaline phosphates.

3.5.1. Effect of acidic phosphate on BOF slag hydration

In the presence of acidic phosphate, an acid-base reaction dominates the early-stage interaction with C_2S , while brownmillerite hydration is inhibited compared to REF, as revealed by QXRD results at 1 day. The reaction proceeds as follows:

$$5 \text{Ca}_2 \text{SiO}_4 + 7 \text{H}_2 \text{PO}_4{}^- \! \to \! 2 \text{Ca}_5 \big(\text{PO}_4 \big)_3 \text{OH} + 5 \text{HSiO}_3{}^- + \text{HPO}_4{}^{2-} + 3 \text{H}_2 \text{O}$$
 (6)

This reaction results in the preferential dissolution of C_2S , leading to the possible formation of calcium phosphate phases, while simultaneously generating silicate species (HSiO $_3$) in solution. However, brownmillerite hydration is suppressed, due to the H₂PO $_4$ /HPO $_4$ -buffering effect, which maintains the system at a pH below 9 (Fig. 3). Similar effects have been reported in C₃A hydration, where phosphoric acid delays dissolution, and hydration only resumes once the system exits the buffering regime [20].

The buffering effect also hinders the precipitation of hydrogarnet and LDHs, as observed in MD at 7 days (Fig. 8 and Fig. 11). While brownmillerite shows a noticeable decline, the expected increase in hydrogarnet and LDHs is limited, suggesting that the low pH environment restricts their formation [20,27].

$3.5.2. \ Effect \ of \ alkaline \ phosphate \ on \ BOF \ slag \ hydration$

In contrast, alkaline phosphate solutions facilitate a different reac-

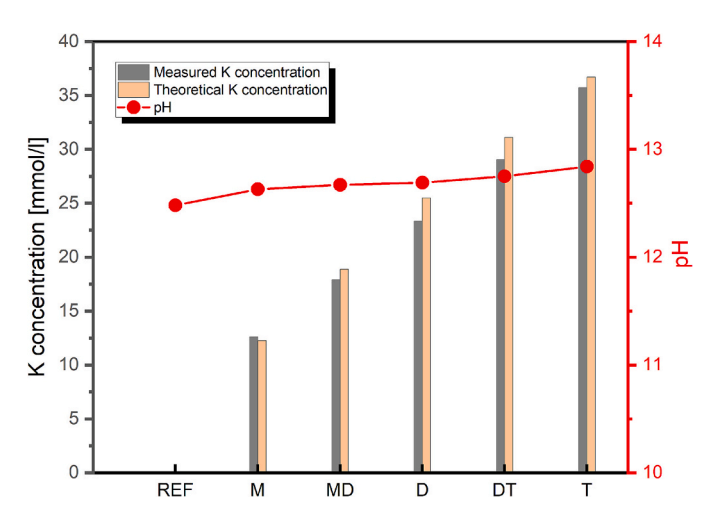


Fig. 16. The pH values and K concentrations from leaching (Note: The measured K concentration in REF is invisible in this figure due to its low value at $\sim 0.1 \, \text{mmol/l}$).

tion pathway, primarily interacting with free Ca^{2+} in the pore solution rather than directly precipitating on the C_2S surface:

$$5Ca^{2+} + 5OH^{-} + 4HPO_{4}^{2-} \rightarrow Ca_{5}(PO_{4})_{3}OH + PO_{4}^{3-} + 4H_{2}O$$
 (7)

$$5Ca^{2+} + OH^{-} + 3PO_{4}^{3-} \rightarrow Ca_{5}(PO_{4})_{3}OH$$
 (8)

This leads to early-stage Ca^{2+} depletion from the solution, and thereby a undersaturation of Ca concentration. Such pathways benefit continuous hydration of C_2S and brownmillerite. Since higher pH levels consume fewer hydroxyl ions during hydroxyapatite formation, the alkalinity of the pore solution increases, further accelerating brownmillerite dissolution. The elevated pH enhances the solubilities of Fe, Al, and Si, facilitating their incorporation into hydrogarnet and C-S-H phases [63–65]. Furthermore, the enhanced hydration of C_2S in alkaline phosphate systems contributes to the stabilization of hydrogarnet, as it supplies sufficient SiO_3^{2-} to substitute OH^- sites, improving the crystallinity and stability of the hydration products [64]. Consequently, phosphate-containing systems with a higher initial pH exhibit shorter induction periods and faster precipitation of hydration products, as evidenced by Fig. 6 and Fig. 8.

4. Conclusions

This study examined the reactions between BOF slag and phosphate across different pH levels, highlighting the effects of acidic and alkaline phosphates on hydration kinetics, microstructure, and strength development. The experimental findings are summarized as follows:

In acidic phosphate solutions, hydration proceeds primarily through an initial acid-base reaction that induces rapid dissolution upon mixing, resulting in lower heat release as detected by calorimetry. In contrast, alkaline phosphate solutions support progressive dissolution-

Leaching of inorganic contaminants measured by one stage batch leaching test and the SQD limit values for unshaped materials.

| 0 0 | , , | U | | | | | | |
|-----------------|-------------------------|--------|--------|--------|--------|--------|--------|--|
| Elements | Unshaped material (SQD) | REF | M | MD | D | DT | T | |
| | [mg/kg] | | | | | | | |
| Barium (Ba) | 22.00 | 0.255 | 0.472 | 0.324 | 0.262 | 0.250 | 0.372 | |
| Chromium (Cr) | 0.63 | bdl* | bdl | 0.001 | bdl | 0.001 | bdl | |
| Molybdenum (Mo) | 1.00 | < 0.01 | < 0.01 | < 0.01 | < 0.01 | < 0.01 | < 0.01 | |
| Vanadium (V) | 1.80 | 0.032 | 0.010 | 0.010 | 0.007 | 0.007 | 0.002 | |
| Zinc (Zn) | 4.50 | < 0.01 | < 0.01 | < 0.01 | < 0.01 | < 0.01 | < 0.01 | |

^{*} bdl-below detection limit. Antimony (Sb), arsenic (As), cadmium (Cd), cobalt (Co), copper (Cu), lead (Pb), nickel (Ni) and tin (Sn) were also undetected by ICP measurement due to the detection limit.

precipitation reactions, leading to continuous hydration and higher cumulative heat. This disparity leads to varying induction periods from several hours to weeks. The retardation effects on hydration diminish with increasing initial pH of phosphate solutions, influenced by the buffering effects of different amounts of $\rm H_2PO_4^-$, $\rm HPO_4^{2-}$, and $\rm PO_4^{3-}$ ions. Once leaving the $\rm H_2PO_4^-/HPO_4^{2-}$ buffering regime, the hydration can still progress. Additionally, this buffering regime impedes the formation of hydrogarnet and LDHs.

At early stage, the reaction extent of C_2S in the samples with acidic phosphates are more pronounced compared to those in samples with alkaline phosphates whereas the hydration of brownmillerite is relatively suppressed. At late stage, higher initial pH leads to greater hydration extent of C_2S , brownmillerite and wuestite for equal phosphate input, accompanied by the formation of more C-S-H, hydrogarnet, and LDHs, which are identified as the main hydration products. These findings are supported by phase composition, chemically bound water, and heat release obtained both from calorimetric measurements and calculations based on reaction enthalpies.

Despite variations in initial pH, the addition of phosphate promotes the hydration of BOF slag at 28 days, optimizing the pore structure. While the overall porosities of all phosphate-containing samples are comparable, ranging from 11.9 to 13.9 %, their strengths vary significantly, with 28-day minimum and maximum strengths between 37.7 and 66.9 MPa. This variation is attributed to a higher proportion of capillary pores and a larger average pore size of 34.7 nm in the sample with low pH (pH 4.2) compared to those with alkaline phosphates. Furthermore, the contradiction between higher hydration extent and lower strength occurs in the sample with pH at 12.8 compared to the sample with lower pH at 11.5, likely due to high K concentration causing shrinkage during air curing.

CRediT authorship contribution statement

Yanjie Tang: Writing – original draft, Methodology, Investigation, Formal analysis, Data curation, Conceptualization. Katrin Schollbach: Writing – review & editing, Supervision. Zixing Liu: Investigation. Sieger van der Laan: Writing – review & editing, Supervision. Wei Chen: Writing – review & editing, Supervision. H.J.H. Brouwers: Writing – review & editing, Supervision.

Declaration of competing interest

The authors declare that they have no known competing financial interests or personal relationships that could have appeared to influence the work reported in this paper.

Acknowledgement

This research is supported by the Department of the Built Environment at Eindhoven University of Technology, Tata steel, M2i (Materials Innovation Institute, project no. T22019). Special thanks are given to Anneke Delsing for her help with ICP and IC tests.

Appendix A. Supplementary data

Supplementary data to this article can be found online at $\frac{https:}{doi.}$ org/10.1016/j.cemconres.2025.108034.

Data availability

Data will be made available on request.

References

 J.J. Schröder, D. Cordell, A.L. Smit, A. Rosemarin, Sustainable Use of Phosphorus Report 357 (European Union Tender Project ENV.B.1/ETU/2009/0025), 2009.

- [2] M. Zhu, Q. Yu, S.R. van der Laan, Y. Chen, Dipotassium hydrogen phosphate activated Al-rich steel slag: the role of layered double hydroxides and aluminum hydrate gel, Cem. Concr. Res. 189 (2025) 107783, https://doi.org/10.1016/j. cemconres 2025 107783
- [3] Y. Tang, Method for Activating Basic Oxygen Furnace Steel Slag, WO 2024/052265 A1, 2024.
- [4] P. Bénard, S. Garrault, A. Nonat, C. Cau-dit-Coumes, Influence of orthophosphate ions on the dissolution of tricalcium silicate, Cem. Concr. Res. 38 (2008) 1137–1141, https://doi.org/10.1016/j.cemconres.2008.03.019.
- [5] P. Bénard, S. Garrault, A. Nonat, C. Cau-Dit-Coumes, Hydration process and rheological properties of cement pastes modified by orthophosphate addition, J. Eur. Ceram. Soc. 25 (2005) 1877–1883, https://doi.org/10.1016/j. jeurceramsoc.2004.06.017.
- [6] T. Zhang, B. Ma, H. Tan, H. Qi, T. Shi, Effect of sodium carbonate and sodium phosphate on hydration of cement paste, J. Build. Eng 45 (2022) 103577, https:// doi.org/10.1016/j.jobe.2021.103577.
- [7] Y. Tang, K. Schollbach, S.R. van der Laan, W. Chen, Activation of BOF slag with dipotassium hydrogen phosphate: enhancing hydration, carbonation resistance, and heavy metal leaching, Cem. Concr. Compos. 157 (2025), https://doi.org/ 10.1016/j.cemconcomp.2025.105922.
- [8] Y. Zhu, Y. Liu, J. Zhang, Monitoring the hydration behavior of hardened cement paste affected by different environmental pH regimes, Front Mater 9 (2022) 1–13, https://doi.org/10.3389/fmats.2022.980887.
- [9] P. Šiler, I. Kolářová, T. Sehnal, J. Másilko, T. Opravil, The determination of the influence of pH value of curing conditions on portland cement hydration, Procedia Eng 151 (2016) 10–17, https://doi.org/10.1016/j.proeng.2016.07.393.
- [10] H. Chen, P. Feng, S. Ye, W. Sun, The coupling effect of calcium concentration and pH on early hydration of cement, Constr. Build. Mater. 185 (2018) 391–401, https://doi.org/10.1016/j.conbuildmat.2018.07.067.
- [11] C.E. Boyd, Water Quality An Introduction, Third edition, 2020.
- [12] K. Scrivener, R. Snellings, B. Lothenbach, F. Group, A Practical Guide to Microstructural Analysis of Cementitious Materials, 2018, https://doi.org/ 10.1201/b19074
- [13] Y. Tang, G. Liu, K. Schollbach, Y. Chen, W. Chen, H.J.H. Brouwers, Re-cementation effects by carbonation and the pozzolanic reaction on LWAs produced by hydrated cement paste powder, J. Clean. Prod. 377 (2022) 134529, https://doi.org/ 10.1016/j.jclepro.2022.134529.
- [14] C.M. Tibbetts, C. Tao, J.M. Paris, C.C. Ferraro, Mercury intrusion porosimetry parameters for use in concrete penetrability qualification using the Katz-Thompson relationship, Constr. Build. Mater. 263 (2020), https://doi.org/10.1016/j. conbuildmat.2020.119834.
- [15] E.W. Washburn, E.W. Washburn, Physics: Note on a Method of Determining the Distribution of Pore Sizes in a Porous Material, https://www.pnas.org, 1921.
- [16] K. Schollbach, S.R. van der Laan, Microstructure Analysis With Quantitative Phase Mapping Using SEM-EDS and Phase Recognition and Characterization (PARC) Software: Applied to Steelmaking Slag, 2022, https://doi.org/10.1515/ 9783110674941-003.
- [17] European Committee for Standardizaiton, EN 12457-1, Characterisation of Waste. Leaching. Compliance Test for Leaching of Granular Waste Materials and Sludges, 2014.
- [18] Q. Wang, Z. Liao, D. Yao, Z. Yang, Y. Wu, C. Tang, Phosphorus immobilization in water and sediment using iron-based materials: a review, Sci. Total Environ. 767 (2021) 144246, https://doi.org/10.1016/j.scitotenv.2020.144246.
- [19] G. Mestres, M.P. Ginebra, Novel magnesium phosphate cements with high early strength and antibacterial properties, Acta Biomater. 7 (2011) 1853–1861, https:// doi.org/10.1016/j.actbio.2010.12.008.
- [20] T. Manninger, D. Jansen, J. Neubauer, F. Goetz-Neunhoeffer, The retarding effect of phosphoric acid during CAC hydration, Cem. Concr. Res. 122 (2019) 83–92, https://doi.org/10.1016/j.cemconres.2019.04.020.
- [21] S.V. Dorozhkin, Calcium orthophosphates (CaPO 4): occurrence and properties, Morphologie 101 (2017) 125–142, https://doi.org/10.1016/j. morpho.2017.03.007.
- [22] C.J. Penn, J.J. Camberato, A critical review on soil chemical processes that control how soil pH affects phosphorus availability to plants, Agriculture (Switzerland) 9 (2019) 1–18, https://doi.org/10.3390/agriculture9060120.
- [23] A. Cuesta, I. Santacruz, S.G. Sanfélix, F. Fauth, M.A.G. Aranda, A.G. De La Torre, Hydration of C4AF in the presence of other phases: a synchrotron X-ray powder diffraction study, Constr. Build. Mater. 101 (2015) 818–827, https://doi.org/ 10.1016/i.conbuildmat.2015.10.114.
- [24] G. Zhang, Q. Ren, J. He, S. Jiang, X. Cheng, Y. Yu, S. Huang, C. Zhang, M. Zhou, New understanding of early hydration of C4AF under surface vitrification, Powder Technol. 377 (2021) 372–378, https://doi.org/10.1016/j.powtec.2020.08.098.
- [25] E. Belhadj, C. Diliberto, A. Lecomte, Characterization and activation of Basic Oxygen Furnace slag, Cem. Concr. Compos. 34 (2012) 34–40, https://doi.org/ 10.1016/j.cemconcomp.2011.08.012.
- [26] A. Cuesta, A. Ayuela, M.A.G. Aranda, Belite cements and their activation, Cem. Concr. Res. 140 (2021) 106319, https://doi.org/10.1016/j. cemconres.2020.106319.
- [27] D.D. Nguyen, L.P. Devlin, P. Koshy, C.C. Sorrell, Effects of acetic acid on early hydration of Portland cement, J. Therm. Anal. Calorim. 123 (2016) 489–499, https://doi.org/10.1007/s10973-015-4942-0.
- [28] B.Z. Dilnesa, E. Wieland, B. Lothenbach, R. Dähn, K.L. Scrivener, Fe-containing phases in hydrated cements, Cem. Concr. Res. 58 (2014) 45–55, https://doi.org/ 10.1016/j.cemconres.2013.12.012.

- [29] F.E. Furcas, B. Lothenbach, O.B. Isgor, S. Mundra, Z. Zhang, U.M. Angst, Solubility and speciation of iron in cementitious systems, Cem. Concr. Res. 151 (2022) 106620, https://doi.org/10.1016/j.cemconres.2021.106620.
- [30] E.M. Gartner, D.E. MacPhee, A physico-chemical basis for novel cementitious binders, Cem. Concr. Res. 41 (2011) 736–749, https://doi.org/10.1016/j. cemconres.2011.03.006.
- [31] T. Matschei, B. Lothenbach, F.P. Glasser, The AFm phase in Portland cement, Cem. Concr. Res. 37 (2007) 118–130, https://doi.org/10.1016/j. cemconres.2006.10.010.
- [32] G. Geng, R.J. Myers, Y.S. Yu, D.A. Shapiro, R. Winarski, P.E. Levitz, D.A. L. Kilcoyne, P.J.M. Monteiro, Synchrotron X-ray nanotomographic and spectromicroscopic study of the tricalcium aluminate hydration in the presence of gypsum, Cem. Concr. Res. 111 (2018) 130–137, https://doi.org/10.1016/j. cemconres.2018.06.002.
- [33] L. Black, C. Breen, J. Yarwood, C.S. Deng, J. Phipps, G. Maitland, Hydration of tricalcium aluminate (C3A) in the presence and absence of gypsum - studied by Raman spectroscopy and X-ray diffraction, J. Mater. Chem. 16 (2006) 1263–1272, https://doi.org/10.1039/b509904h.
- [34] W. Franco Santos, K. Schollbach, S. Melzer, S.R. van der Laan, H.J.H. Brouwers, Quantitative analysis and phase assemblage of basic oxygen furnace slag hydration, J. Hazard. Mater. 450 (2023) 131029, https://doi.org/10.1016/j. ibazmat.2023.131029.
- [35] J. Vecstaudza, M. Gasik, J. Locs, Amorphous calcium phosphate materials: formation, structure and thermal behaviour, J. Eur. Ceram. Soc. 39 (2019) 1642–1649, https://doi.org/10.1016/j.jeurceramsoc.2018.11.003.
- [36] A.M. Kaja, K. Schollbach, S. Melzer, S.R. van der Laan, H.J.H. Brouwers, Q. Yu, Hydration of potassium citrate-activated BOF slag, Cem. Concr. Res. 140 (2021) 106291, https://doi.org/10.1016/j.cemconres.2020.106291.
- [37] E. Sassoni, E. Franzoni, Lime and cement mortar consolidation by ammonium phosphate, Constr. Build. Mater. 245 (2020) 118409, https://doi.org/10.1016/j. conbuildmat.2020.118409.
- [38] I.A. Karampas, C.G. Kontoyannis, Characterization of calcium phosphates mixtures, Vib. Spectrosc. 64 (2013) 126–133, https://doi.org/10.1016/j. vibspec.2012.11.003.
- [39] A. Blandine Loth, M. Vincent, G. Ellis, Hydration of Belite-Ye' elimite-Ferrite cements: thermodynamic modeling, in: 14th International Congress on the Chemistry of Cement (ICCC), 2015.
- [40] L.U.D. Tambara, M. Cheriaf, J.C. Rocha, A. Palomo, A. Fernández-Jiménez, Effect of alkalis content on calcium sulfoaluminate (CSA) cement hydration, Cem. Concr. Res. 128 (2020) 105953, https://doi.org/10.1016/j.cemconres.2019.105953.
- [41] D. Ectors, J. Neubauer, F. Goetz-Neunhoeffer, The hydration of synthetic brownmillerite in presence of low Ca-sulfate content and calcite monitored by quantitative in-situ-XRD and heat flow calorimetry, Cem. Concr. Res. 54 (2013) 61–68, https://doi.org/10.1016/j.cemconres.2013.08.011.
- [42] M.J. Ahmed, K. Lambrechts, X. Ling, K. Schollbach, H.J.H. Brouwers, Effect of hydroxide, carbonate, and sulphate anions on the β-dicalcium silicate hydration rate, Cem. Concr. Res. 173 (2023), https://doi.org/10.1016/j. cemconres 2023 107302
- [43] A.M. Kaja, S. Melzer, H.J.H. Brouwers, Q. Yu, On the optimization of BOF slag hydration kinetics, Cem. Concr. Compos. 124 (2021) 104262, https://doi.org/ 10.1016/j.cem.concomp.2021.104262.
- [44] K. Schollbach, M.J. Ahmed, S.R. van der Laan, The mineralogy of air granulated converter slag, Int. J. Ceram. Eng. Sci. 3 (2021) 21–36, https://doi.org/10.1002/ ces2.10074
- [45] K.D. Grevel, F. Bellmann, J. Majzlan, E. Dachs, A. Benisek, H.M. Ludwig, Thermodynamic data of belite polymorphs, Cem. Concr. Res. 152 (2022) 106621, https://doi.org/10.1016/j.cemconres.2021.106621.
- [46] X. Jia, J. Li, P. Wang, J. Qian, M. Tang, Preparation and mechanical properties of magnesium phosphate cement for rapid construction repair in ice and snow, Constr. Build. Mater. 229 (2019) 116927, https://doi.org/10.1016/j. conbuildmat.2019.116927.
- [47] B. Lothenbach, D.A. Kulik, T. Matschei, M. Balonis, L. Baquerizo, B. Dilnesa, G. D. Miron, R.J. Myers, Cemdata18: A chemical thermodynamic database for

- hydrated Portland cements and alkali-activated materials, Cem. Concr. Res. 115 (2019) 472–506, https://doi.org/10.1016/j.cemconres.2018.04.018.
- [48] H.F.W. Taylor, Cement Chemistry, 2nd ed, Academic Press, 1997, https://doi.org/ 10.1016/S0958-9465(98)00023-7.
- [49] Q. Li, Z. Liu, W. Chen, B. Yuan, X. Liu, W. Chen, A novel bio-inspired bone-mimic self-healing cement paste based on hydroxyapatite formation, Cem. Concr. Compos. 104 (2019) 103357, https://doi.org/10.1016/j. cemconcomp.2019.103357.
- [50] B. Xu, F. Winnefeld, B. Lothenbach, Effect of temperature curing on properties and hydration of wollastonite blended magnesium potassium phosphate cements, Cem. Concr. Res. 142 (2021) 106370, https://doi.org/10.1016/j. cemconres.2021.106370.
- [51] M. Tonsuaadu, K. Gross, K.A. Plūduma, L. Veiderma, A review on the thermal stability of calcium apatites, J. Therm. Anal. Calorim. 110 (2012) 647–956.
- [52] M.D. Mullen, Phosphorus in soils biological interactions, in: Encyclopedia of Soils in the Environment 4, 2004, pp. 210–216, https://doi.org/10.1016/B0-12-348530-4/00161-2.
- [53] H. Mehdizadeh, X. Cheng, K.H. Mo, T.C. Ling, Upcycling of waste hydrated cement paste containing high-volume supplementary cementitious materials via CO2 pretreatment, J. Build. Eng 52 (2022) 104396, https://doi.org/10.1016/j. jobe.2022.104396.
- [54] T. Kubota, A. Nakamura, K. Toyoura, K. Matsunaga, The effect of chemical potential on the thermodynamic stability of carbonate ions in hydroxyapatite, Acta Biomater. 10 (2014) 3716–3722, https://doi.org/10.1016/j.actbio.2014.05.007.
- [55] S.P. Parthiban, I.Y. Kim, K. Kikuta, C. Ohtsuki, Effect of ammonium carbonate on formation of calcium-deficient hydroxyapatite through double-step hydrothermal processing, J. Mater. Sci. Mater. Med. 22 (2011) 209–216, https://doi.org/ 10.1007/s10856-010-4201-7.
- [56] T. Wang, A. Dorner-Reisel, E. Müller, Thermogravimetric and thermokinetic investigation of the dehydroxylation of a hydroxyapatite powder, J. Eur. Ceram. Soc. 24 (2004) 693–698, https://doi.org/10.1016/S0955-2219(03)00248-6.
- [57] G. Sant, A. Kumar, C. Patapy, G. Le Saout, K. Scrivener, The influence of sodium and potassium hydroxide on volume changes in cementitious materials, Cem. Concr. Res. 42 (2012) 1447–1455, https://doi.org/10.1016/j. cemconres.2012.08.012.
- [58] A.M. Kaja, A. Delsing, S.R. van der Laan, H.J.H. Brouwers, Q. Yu, Effects of carbonation on the retention of heavy metals in chemically activated BOF slag pastes, Cem. Concr. Res. 148 (2021) 106534, https://doi.org/10.1016/j. cemconres.2021.106534.
- [59] M.J. Ahmed, R. Cuijpers, K. Schollbach, S.R. van der Laan, M. Van Wijngaarden-Kroft, T. Verhoeven, H.J.H. Brouwers, V and Cr substitution in dicalcium silicate under oxidizing and reducing conditions – synthesis, reactivity, and leaching behavior studies, J. Hazard. Mater. 442 (2023) 130032, https://doi.org/10.1016/j. ibazmat.2022.130032.
- [60] A. van Zomeren, S.R. van der Laan, H.B.A. Kobesen, W.J.J. Huijgen, R.N. J. Comans, Changes in mineralogical and leaching properties of converter steel slag resulting from accelerated carbonation at low CO 2 pressure, Waste Manag. 31 (2011) 2236–2244, https://doi.org/10.1016/j.wasman.2011.05.022.
- [61] G. Costa, A. Polettini, R. Pomi, A. Stramazzo, Leaching modelling of slurry-phase carbonated steel slag, J. Hazard. Mater. 302 (2016) 415–425, https://doi.org/ 10.1016/j.jhazmat.2015.10.005.
- [62] Y. Yan, S.Y. Yang, G.D. Miron, I.E. Collings, E. L'Hôpital, J. Skibsted, F. Winnefeld, K. Scrivener, B. Lothenbach, Effect of alkali hydroxide on calcium silicate hydrate (C-S-H), Cem. Concr. Res. 151 (2022), https://doi.org/10.1016/j. cemconres 2021 106636
- [63] E. Wieland, G.D. Miron, B. Ma, G. Geng, B. Lothenbach, Speciation of iron(II/III) at the iron-cement interface: a review, Mater. Struct 56 (2023), https://doi.org/ 10.1617/s11527-023-02115-x
- [64] B.Z. Dilnesa, B. Lothenbach, G. Renaudin, A. Wichser, D. Kulik, Synthesis and characterization of hydrogarnet Ca3(Al xFe1 - X)2(SiO4)y(OH) 4(3 - y), Cem. Concr. Res. 59 (2014) 96–111, https://doi.org/10.1016/j.cemconres.2014.02.001.
- [65] P.V. Brady, J.V. Walther, Controls on silicate dissolution rates in neutral and basic pH solutions at 25°C, Geochim. Cosmochim. Acta 53 (1989) 2823–2830, https://doi.org/10.1016/0016-7037(89)90160-9.